SEISMIC CHARACTERIZATION OF RESERVOIRS WITH MULTIPLE FRACTURE SETS USING VELOCITY AND ATTENUATION ANISOTROPY DATA

Aamir Ali[1] and Morten Jakobsen[1, 2]

[1]Department of Earth Sciences, University of Bergen, Allegaten 41, 5007 Bergen, Norway.

[2]Centre for Integrated Petroleum Research, University of Bergen, Allegaten 41, 5007 Bergen, Norway.

Abstract

Knowledge about the spatial distribution of the fracture density and the azimuthal fracture orientation can greatly help in optimizing production from fractured reservoirs. Frequency-dependent seismic velocity and attenuation anisotropy data contain information about the fractures present in the reservoir. In this study, we use the measurements of velocity and attenuation anisotropy data corresponding to different seismic frequencies and azimuths to infer information about the multiple fracture sets present in the reservoir. We consider a reservoir model with two sets of vertical fractures characterized by unknown azimuthal fracture orientations and fracture densities. Frequency-dependent seismic velocity and attenuation anisotropy data is computed using the effective viscoelastic stiffness tensor and solving the Christoffel equation. A Bayesian inversion method is then applied to measurements of velocity and attenuation anisotropy data corresponding to different seismic frequencies and azimuth to estimate the azimuthal fracture orientations and the fracture densities, as well as their uncertainties. Our numerical examples suggest that velocity anisotropy data alone cannot recover the unknown fracture parameters. However, an improved estimation of the unknown fracture parameters can be obtained by joint inversion of velocity and attenuation anisotropy data.

Keywords: Frequency-dependent seismic anisotropy, Seismic attenuation, Seismic Bayesian inversion, Multiple fracture sets

1 Introduction

The successful management of fractured reservoirs depends upon improved characterization of fracture systems which often provide pathways for fluid flow during production. Alignment of these fracture systems to preferred orientations will lead to anisotropic wave characteristics and permeability in the reservoir. This suggests the use of seismic anisotropy to determine the orientation of fractures (Sayers, 2009). Knowledge about the spatial distribution of fracture density and azimuthal fracture orientation can greatly help in optimizing production from fractured reservoirs (Sayers, 2009). Frequency-dependence of seismic velocity and attenuation anisotropy data can potentially give important information about the fracture systems (Chapman, 2003; Liu et al., 2006; Liu et al., 2007a, b; Maultzsch et al., 2007a, b; Chapman, 2009; Gurevich et al., 2009).

Wave induced fluid flow and multiple scattering are believed to be the main driving mechanisms behind the attenuation of seismic waves. Scattering attenuation can be safely ignored in the long wavelength domain i.e. when fractures are much smaller than the seismic wavelength. This is due to the fact that the propagating seismic wave or flowing fluid only sees a homogenized structure and not the individual pores, micro-cracks or mesoscopic fractures. Wave induced fluid flow can occur at microscopic scale of pores and micro-cracks, the mesoscopic scale of fractures and the macroscopic scale of seismic wavelengths (Chapman, 2003; Gurevich et al., 2009). In particular, wave induced fluid flow caused by the pressure gradients at the microscopic or mesoscopic scale and in a direction potentially different from that of the wave propagation is known as squirt flow, whereas the wave induced fluid flow caused by the pressure gradients at the scale of the acoustic wavelength and in the direction of the wave propagation is known as global or Darcy flow.

The objective of this study is to infer more information about multiple fracture systems using measurements of velocity and attenuation anisotropy data corresponding to different seismic frequencies and azimuths. This has been done by some authors before in the context of forward modelling (see Liu et al., 2006; Liu et al., 2007a, b; Chapman, 2009). In this paper we study the inverse as well as the forward modelling.

We use the viscoelastic T-matrix approach of Jakobsen et al. (2003b) and Jakobsen and Chapman (2009), which is the most general model among the inclusion models, because it allows for non-dilute concentration of cavities characterized by different shapes, orientations and spatial distributions (see Gurevich et al., 2009; Müller et al., 2010). In addition to that the theory of Jakobsen and Chapman (2009) takes into account global and squirt flow in a consistent manner. We have also given attention to the discrimination of micro-cracks and mesoscopic fractures. The discrimination of micro-cracks and mesoscopic fractures is very important, because the analysis of seismic anisotropy data based upon static effective medium theories always assumes frequency-independence and cannot discriminate between them (Maultzsch et al., 2003). Numerical examples are presented about the inverse problem of estimating the fracture parameters (azimuthal fracture orientations and the fracture densities) from measurements of velocity and attenuation anisotropy corresponding to different seismic frequencies and azimuths using a Monte Carlo Markov chain (MCMc) inversion in a Bayesian setting.

2 The effective viscoelastic stiffness tensor

We depict a fractured reservoir as being composed of a solid matrix with a population of cavities. The population of cavities is divided into N families, where members in each family have the same shape, orientation, scale-size and volume concentration $v^{(r)}$ labeled by $r = 1,...,R$. The different families of the cavities considered in this study are pores, randomly oriented micro-cracks and two sets of aligned mesoscopic fractures. Formally, randomly

oriented micro-cracks mean infinitely many families or sets, but we perform an averaging over the different orientations (see Jakobsen *et al*. 2003a, b). The fracture volume concentration $v^{(r)}$ is related to the fracture density $\varepsilon^{(r)}$ by $v^{(r)} = (4/3)\pi\varepsilon^{(r)}\alpha^{(r)}$, where $\alpha^{(r)}$ is aspect ratio for fractures of type r. The aspect ratio of a spheroidal cavity with long (short) axis $a^{(r)}$ ($c^{(r)}$) is given by $c^{(r)}/a^{(r)}$. The fracture density $\varepsilon^{(r)}$ is defined by $\varepsilon^{(r)} = N(a^{(r)})^3$, where N is the number density of fractures of type r within a representative volume element. The effective stiffness tensor $\mathbf{C}^*$ is given by (Jakobsen et al., 2003a, b)

$$\mathbf{C}^* = \mathbf{C}^{(0)} + \mathbf{C}_1 : (\mathbf{I}_4 + \mathbf{C}_1^{-1} : \mathbf{C}_2)^{-1}, \tag{1}$$

where

$$\mathbf{C}_1 = \sum_{r=1}^{N} v^{(r)} \mathbf{t}^{(r)}, \tag{2}$$

and

$$\mathbf{C}_2 = \sum_{r=1}^{N}\sum_{s=1}^{N} v^{(r)} \mathbf{t}^{(r)} : \mathbf{G}_d^{(rs)} : \mathbf{t}^{(s)} v^{(s)}. \tag{3}$$

Here, $\mathbf{C}^{(0)}$ represents the elastic properties of the solid matrix, : denotes the double scalar product (see Auld 1990), $\mathbf{I}_4$ is the (symmetric) identity for fourth-rank tensors and $\mathbf{G}_d^{(rs)}$ is given by the strain Green's function integrated over an ellipsoid having the same aspect ratio as $p^{(s|r)}(\mathbf{x} - \mathbf{x}')$, which in turn gives the probability density for finding an inclusion of type s at $\mathbf{x}'$, given that there is an inclusion of type r at point $\mathbf{x}$ (Jakobsen et al., 2003a, b). It is generally assumed that the correlation function has ellipsoidal or spherical symmetry represented by the choice of aspect ratios. In this study, we have also assumed the aspect ratio of the correlation function equal to 1 i.e. $\alpha_d = 1$. This represents a uniform spatial distribution of fractures with spherically symmetric correlation function.

The t-matrix for a cavity of type r fully saturated with a homogenous fluid can be written as (Jakobsen et al., 2003b; Jakobsen and Chapman, 2009; Appendix-A)

$$\mathbf{t}^{(r)} = \mathbf{t}^{(r)}(\mathbf{v}, \boldsymbol{\Omega}, \boldsymbol{\alpha}, k_f, \eta_f, \mathbf{K}^*, \boldsymbol{\tau}) \ ; \qquad r = (1,...,R), \tag{4}$$

where $\mathbf{v} = (v^{(1)},...,v^{(n)})$ is a vector with the volume concentration for each cavity set, $\boldsymbol{\Omega} = (\Omega^{(1)},...,\Omega^{(n)})$ denotes the Euler's angles determining the orientation of each cavity set relative to the crystallographic axes of the material with properties given by $\mathbf{C}^{(0)}$, $\boldsymbol{\alpha} = (\alpha^{(1)},...,\alpha^{(n)})$ is a vector with the aspect ratios for each cavity set, k_f is the bulk modulus of the saturating fluid, η_f is the viscosity of the fluid, $\mathbf{K}^*$ is the effective permeability tensor and $\boldsymbol{\tau} = (\tau^{(1)},...,\tau^{(n)})$ is a vector with the relaxation time constants for each cavity set.

For a reservoir model consisting of two aligned mesoscopic fracture sets with unknown azimuthal fracture orientations and fracture densities (as assumed in this study), we can write $\mathbf{t}^{(r)}$ as

$$\mathbf{t}^{(r)} = \mathbf{t}^{(r)}(\psi_1, \psi_2, \varepsilon_1, \varepsilon_2)\,. \tag{5}$$

Here, ψ_1 and ψ_2 represent the azimuthal fracture orientation of each fracture set and ε_1 and ε_2 represent the fracture density of each fracture set. The viscoelastic T-matrix approach of Jakobsen et al. (2003b) and Jakobsen and Chapman (2009) to cracked/fractured porous media with an improvement is given in appendix-A. This improvement is related to relaxing on the assumption that the inclusions or cavities are of the same scale-size (see appendix-A). The relaxation time of fractures τ_f can be calculated according to their size from the following equation (Chapman 2003; Agersborg et al., 2007)

$$\tau_f = \frac{r}{\xi}\tau_m\,. \tag{6}$$

Here, r is the radius of fractures, ξ is the size of the grains and τ_m is the relaxation time for the micro-porosity. The theory of Jakobsen and Chapman (2009) predicts a frequency dependence of the seismic anisotropy by modelling the velocity dispersion and attenuation caused by squirt and global flow mechanisms for micro-porosity and mesoscopic fractures.

In general, $\mathbf{C}^*$ depends on effective wave vector $\mathbf{k}^*$ and angular frequency ω. However, following Hudson et al., 1996, Pointer et al., 2000, Tod, 2001, Jakobsen et al., 2003b and Jakobsen and Chapman (2009), we eliminate the dependency of $\mathbf{C}^*$ on the effective wave vector $\mathbf{k}^*$ by using the approximation $k^* = k \approx \omega / V^{(0)}$, where $V^{(0)}$ is the speed of the wave mode under consideration in the solid matrix and k is the length of $\mathbf{k}$. In this approach of using an approximation for effective wave vector, the effective permeability tensor $\mathbf{K}^*$ of the fractured reservoir is taken equal to the matrix permeability of the reservoir.

For the two mesoscopic fracture sets embedded in the solid matrix with different orientations, the symmetry of the rock is monoclinic and therefore characterized by 13 independent viscoelastic stiffness coefficients. The components of the effective viscoelastic stiffness tensor are a function of the fracture parameters, which is given by viscoelastic rock physics modelling as discussed above. The non-vanishing viscoelastic stiffness constants of a medium of monoclinic symmetry (see appendix-B) in the usual two-index notation are c_{11}, c_{22}, c_{33}, $c_{12} = c_{21}$, $c_{13} = c_{31}$, $c_{23} = c_{32}$, c_{44}, c_{55}, c_{66}, $c_{16} = c_{61}$, $c_{26} = c_{62}$, $c_{36} = c_{63}$ and $c_{45} = c_{54}$. The presence of mesoscopic fractures present in a reservoir can produce significant dispersion and attenuation at seismic frequencies (Maultzsch et al., 2003; Liu et al., 2007a, b; Gurevich et al., 2009).

Figure 1 and 2 show the real and imaginary parts of the 13 independent effective stiffness constants as a function of seismic frequency for three different combinations of azimuthal fracture orientations and fracture densities of each individual fracture set. Both the real and imaginary parts of independent effective stiffness constants show a high sensitivity to changes in azimuthal fracture orientations and fracture densities of both the fracture sets. We observe squirt flow characterized by positive dispersion (figure 1) and corresponding attenuation (figure 2) at seismic frequencies ($\leq 10^2$ Hz) for the effects associated with the

presence of mesoscopic fracture sets, and at higher frequencies (between 10^3 to 10^5 Hz) for the effects associated with micro-porosity (pores and micro-cracks) for effective stiffness constants c_{11}, c_{22}, c_{33}, c_{12}, c_{13}, c_{23}, c_{66}. We only observe positive dispersion (figure 1) and corresponding attenuation (figure 2) associated with the effects of micro-porosity for the effective stiffness constants c_{44} and c_{55}. For the effective stiffness constants c_{16}, c_{26} and c_{36}, we observe both positive and negative dispersion (figure 1) and corresponding attenuation (figure 2) at seismic frequencies. No dispersion either positive or negative is observed for the effective stiffness constant c_{45}. The values of effective stiffness constants c_{16}, c_{26}, c_{36} and c_{45} can be both positive or negative, depending on the azimuthal orientation of the coordinate system relative to the fracture normal.

Figures 3 and 4 show the real and imaginary parts of the independent effective stiffness constants as a function of azimuthal fracture orientations of two fracture sets for a fixed frequency of 40 Hz. Both the real and imaginary parts of the effective stiffness constants vary more or less periodic with the azimuthal fracture orientations, in accordance with the transformation laws for fourth-rank tensors (Auld, 1990).

Figures 5 and 6 shows the real and imaginary parts of the independent effective stiffness constants as a function of fracture densities of two fracture sets for a fixed frequency of 40 Hz. The real parts of effective stiffness constants decrease with increasing fracture density except the effective stiffness constants c_{16}, c_{26}, c_{36} and c_{45} that can increase or decrease with increasing fracture density depending on the azimuthal orientation of the coordinate system relative to the fracture normal. The imaginary parts of effective stiffness constants increase with increasing fracture density except the effective stiffness constants c_{44}, c_{55}, c_{16}, c_{26}, c_{36} and c_{45} that can increase or decrease with increasing fracture density depending on the azimuthal orientation of the coordinate system relative to the fracture normal.

3 Forward modelling of seismic velocity and attenuation anisotropy

3.1 The non-linear forward model

The non-linear forward model can be written as:

$$\mathbf{d} = \mathbf{G}(\mathbf{m}). \tag{7}$$

Here **m** is a vector of model parameters related to the fractures (the azimuthal fracture orientations (ψ_1 and ψ_2) and the fracture densities (ε_1 and ε_2)). The function **G** is based on a combination of the viscoelastic rock physics model and seismic attribute generation (predictions of velocity and attenuation anisotropy data corresponding to different seismic frequencies and azimuths). **d** is a vector of observable quantities (measurements of velocity and attenuation anisotropy data corresponding to different seismic frequencies and azimuths).

The azimuthal variation of frequency-dependent velocity and attenuation anisotropy data can provide useful information about the fracture systems present in the reservoir (Liu et al., 2006; Liu et al., 2007a, b; Maultzsch et al., 2007a, b; Chapman, 2009). But first we need to discuss how to obtain real-valued phase velocities and attenuation spectra from the frequency-dependent and complex-valued effective stiffness tensor $\mathbf{C}^*$. The real-valued phase velocities and attenuation factors can be obtained by inserting the effective stiffness tensor $\mathbf{C}^*$ into the Christoffel equation (see appendix-C), which can be solved by computing the eigenvectors and eigenvalues (Jakobsen et al., 2003b; Carcione, 1995, 2007). More detailed information about the plane waves in viscoelastic anisotropic media can be obtained from Cerveny and Psencik (2005). The phase velocity is the reciprocal of the slowness and in component form is given by (Carcione, 1995, 2007)

$$\mathbf{V}_p = \left(\mathrm{Re}\left[\frac{1}{V} \right] \right)^{-1} \hat{\mathbf{I}}. \tag{8}$$

The quality factor Q is defined as the ratio of the peak strain energy to the average loss energy density (Auld, 1990), and is defined by (Carcione, 1995, 2007)

$$Q = \frac{\mathrm{Re}(V^2)}{\mathrm{Im}(V^2)}. \tag{9}$$

3.2 Forward modelling results and discussion

In this section we show some forward numerical calculations to infer important information about multiple fracture sets using velocity and attenuation anisotropy data for different seismic frequencies and azimuths. For the background elastic parameters, the properties of the calcite are used to obtain the stiffness tensor for the solid matrix $\mathbf{C}^{(0)}$. The porosity for spherical pores is 8%, while crack density for randomly oriented micro-cracks is 0.05, respectively. The rock is assumed to be fully saturated with water. The mechanical properties of the solid matrix and fluid (brine/water) are given in Table 1. The viscosity of water (the saturating fluid) is 10^{-3} Pa s (see Pointer et al., 2000) and matrix permeability is100 mD. The relaxation time constant τ_m is same for the pores and micro-cracks in the micro-porosity which can be found from the core plug velocity and attenuation measurements and set to 2×10^{-7} s. The size of the grains ξ is assumed to be known and set to 200×10^{-6} m.

Model 0. Single set of aligned mesoscopic fractures

We first consider the model where we have one set of aligned mesoscopic fractures along with pores and randomly oriented micro-cracks (micro porosity) having a fracture density of 0.08 and aspect ratio of 0.001. The fracture radius is 0.1m and from equation (6), the relaxation time τ_f for one fracture set will be equal to 10^{-4} s. Figure 7 shows the azimuthal variation of P-wave velocity and attenuation for 4 different seismic frequencies and a fixed polar angle of incidence (40^o) in a medium with one mesoscopic fracture set. There is a correlation between the maximum and minimum of velocity and attenuation spectra as a function of azimuth. The azimuthal orientation of the mesoscopic fracture set is 40^o (see appendix-B). The azimuth of maximum velocity coincides with the azimuth of minimum

attenuation i.e. around 40^o. The azimuth of minimum velocity observed at an azimuth of around 130^o will again correspond to the azimuth of maximum attenuation.

Model 1. Two sets of aligned mesoscopic fractures

We now consider the model where we have two sets of aligned mesoscopic fractures along with pores and randomly oriented micro-cracks (micro-porosity) having the same fracture density and aspect ratio of 0.08 and 0.001, respectively. The fracture radius of both the mesoscopic fracture sets is 0.1 m, corresponding to the squirt flow relaxation time for each of the fracture sets equal to 10^{-4} s (equation (6)).

Figure 8 shows the azimuthal variation of P-wave velocity and attenuation for 4 different seismic frequencies and a fixed polar angle of incidence (40^o) in a medium with two mesoscopic fracture sets. The azimuthal orientations of the two mesoscopic fracture sets are 40^o and 110^o (see appendix-B). Again we note the correlation between the maximum and minimum azimuth of velocity and attenuation. The maximum velocity and minimum attenuation occurs at an azimuth of around 75^o which is the weighted average of the azimuthal orientations of both the mesoscopic fracture sets. This result also has an important implication in the context of seismic fracture characterization in a sense that the analysis of seismic data based on a model assuming a single set of aligned mesoscopic fracture set can sometimes give the misleading results.

The forward modelling performed using model 2 can also predict qualitatively same behavior for velocity and attenuation spectra in the absence of randomly oriented micro-cracks as obtained by Chapman (2009) for pores and two sets of aligned mesoscopic fracture sets.

Model 2. Aligned micro-cracks and mesoscopic fractures

In this model, we let one mesoscopic fracture set having an azimuthal orientation of 110^o in model 2 to become aligned micro-cracks by setting its relaxation time same as for the

micro-porosity. This is an interesting case because now there is no correlation between maximum and minimum of velocity and attenuation as a function of azimuth (figure 9). We observe a maximum velocity around 75^o-100^o azimuth and minimum attenuation around 40^o azimuth depending on the frequency. The azimuthal variation of attenuation is now only sensitive to the mesoscopic fracture set having an azimuthal orientation of 40^o. This also indicates that attenuation data can help in solving the non-uniqueness in the azimuthal orientations for this particular case.

The forward modelling performed using model 3 can also be used to model the open (supports fluid communication) and sealed fracture sets (no fluid communication) as discussed by the Chapman (2009). The azimuthal variation of attenuation will only be sensitive to the open fracture set, while directional variation of velocity as a function of azimuth will be observed, respectively. The presence of open and sealed fracture sets will qualitatively give the same behavior for azimuthal variation of velocity and attenuation as obtained by the presence of aligned micro-cracks and a mesoscopic fracture set.

4 Inversion of velocity and attenuation anisotropy data

4.1 Bayesian approach

We define the non-linear inverse problem by

$$\mathbf{G}(\mathbf{m}) \approx \mathbf{d} + \boldsymbol{\eta}. \tag{10}$$

Here **d** is a vector of observable quantities (measurements of velocity and attenuation data corresponding to different seismic frequencies and azimuths) and **G** is a combination of viscoelastic rock physics modelling and the relations of velocity and attenuation to obtain the predictions of velocity and attenuation anisotropy data corresponding to different seismic frequencies and azimuths. **m** is a vector of model parameters related with fractures (the azimuthal fracture orientations (ψ_1 and ψ_2) and the fracture densities (ε_1 and ε_2) and in the

inverse problem estimated using $\mathbf{G}$ and $\mathbf{d}$. $\boldsymbol{\eta}$ is the noise vector and normally it is assumed to be Gaussian.

There are different approaches to solve an inverse problem and in this study we have used Bayesian approach (Aster et al., 2005; Tarantola, 2005). The solution to the inverse problem is given by the posterior distribution $q(\mathbf{m}|\mathbf{d})$ over the model space *M*. We use Bayes' theorem to define the posterior distribution, which relates the prior and posterior distributions in a way that makes the computation of $q(\mathbf{m}|\mathbf{d})$ possible. Bayes' theorem can be stated as follows (Aster et al., 2005)

$$q(\mathbf{m}\,|\,\mathbf{d}) \propto f(\mathbf{d}\,|\,\mathbf{m})p(\mathbf{m}), \tag{11}$$

where $f(\mathbf{d}\,|\,\mathbf{m})$ is the likelihood that given a particular model **m**, a data vector, **d**, will be observed and $p(\mathbf{m})$ is the prior distribution of the model parameters. The velocity and attenuation data enter into the formulation through the likelihood $f(\mathbf{d}\,|\,\mathbf{m})$, which determines the conditional probability density for the observed data given the values of the model parameters. The prior probability density $p(\mathbf{m})$ is based on the information which is found independently of the seismic velocities and attenuation data. Limited information about the fracture density about the fracture densities and azimuthal orientations at inter-well locations can be obtained from observations and interpolation of borehole data. Also, the use of outcrop analogues can provide limited (a priori) information about the parameters of fractures. In addition, information about in-situ stress field may provide some clues to the orientation and density of the open fractures within a fractured reservoir. If we have an uninformative prior as assumed in this study also, then equation (11) becomes (Aster et al., 2005)

$$q(\mathbf{m}\,|\,\mathbf{d}) \propto f(\mathbf{d}\,|\,\mathbf{m}), \tag{12}$$

and the posterior distribution is precisely the likelihood function, $L(\mathbf{m}\,|\,\mathbf{d})$. The likelihood $L(\mathbf{m}\,|\,\mathbf{d})$ of a given model $\mathbf{m}$ is measured through its misfit or objective function $J(\mathbf{m})$ which in the case of Gaussian statistics is given by (Aster et al., 2005)

$$J(\mathbf{m}) = \frac{1}{2}\left[(\mathbf{G}(\mathbf{m}) - \mathbf{d})^T \mathbf{C}_D^{-1} (\mathbf{G}(\mathbf{m}) - \mathbf{d})\right], \tag{13}$$

where the covariance matrix $\mathbf{C}_D$ contains information about the measurement errors. The following solution of posterior distribution is now obtained from the above equations (Aster et al., 2005)

$$q(\mathbf{m}\,|\,\mathbf{d}) \propto \exp(-J(\mathbf{m})). \tag{14}$$

To quantify the uncertainty in the inverted model parameters the exploration of the posterior PDF can be done by Monte Carlo sampling. We have adapted the Metropolis algorithm (Tarantola, 2005) to the problem of sampling the posterior probability density in this study.

Suppose that at a given step, the random walker is at point $\mathbf{m}_i$, and the application to rules would lead to a transition to point $\mathbf{m}_j$. Sometimes we reject this proposed transition by using the following rule (Tarantola, 2005):

(1) If $L(\mathbf{m}_j\,|\,\mathbf{d}) \geq L(\mathbf{m}_i\,|\,\mathbf{d})$, then accept the proposed transition to $\mathbf{m}_j$.

(2) If $L(\mathbf{m}_j\,|\,\mathbf{d}) < L(\mathbf{m}_i\,|\,\mathbf{d})$, then decide randomly to move to $\mathbf{m}_j$, or to stay at $\mathbf{m}_i$, with the following probability of accepting to move to $\mathbf{m}_j$.

$$P_{i\to j} = \frac{L(\mathbf{m}_j\,|\,\mathbf{d})}{L(\mathbf{m}_i\,|\,\mathbf{d})}. \tag{15}$$

Then the random walker samples the posteriori probability density $q(\mathbf{m}\,|\,\mathbf{d})$. There is no general rule for obtaining the independent posterior samples, as this strongly depends on the particular problem at hand. The other important point to emphasize is the acceptance rate of the Metropolis criterion, which should not be too small and too large (Tarantola, 2005). This

acceptance rate determines the efficiency of the Monte Carlo Markov chain (MCMc). If the acceptance rate is larger, we are not moving fast enough in the model space; if it is smaller, we are wasting our resources to test models that are not accepted (Tarantola, 2005).

4.2 Inverse modelling results and discussion

In this section we perform inverse numerical experiments to investigate to what extent one can recover fracture parameters (the azimuthal fracture orientations (ψ_1 and ψ_2) and fracture densities (ε_1 and ε_2) using the measurements of velocity and attenuation anisotropy data corresponding to different seismic frequencies and azimuths. The different background parameters are same as discussed in the section 3. The lengths of the two mesoscopic fracture sets are assumed to be known from geologic outcrops field analogues and well log data and set to 0.2 m. The aspect ratios of the two mesoscopic fracture sets are set to 0.001. For the calculated velocity and attenuation data we have used the rock physics model discussed in section 2.1 to obtain the viscoelastic stiffness tensor and then used the relations of velocity and attenuation discussed in section 3 to obtain the measurements of velocity and attenuation anisotropy data corresponding to different seismic frequencies and azimuths for a fixed polar angle of incidence (40^o).

Figure 10 shows an example of predictions of velocity and attenuation as a function of fracture parameters for a fixed seismic frequency (40 Hz) and azimuth (45^o). Figure 11 shows an example of synthetic velocity and attenuation data as a function of seismic frequency and azimuth used for inversion in this study.

Model 1. Two sets of aligned mesoscopic fractures

Our first inverse numerical example deals with the model 1 of the forward modelling section. We invert for the azimuthal fracture orientations (ψ_1 and ψ_2) and fracture densities (ε_1 and ε_2) of the two aligned mesoscopic fracture sets using measurements of velocity

anisotropy data alone and using both velocity and attenuation anisotropy data corresponding to different seismic frequencies and azimuths. The true azimuthal fracture orientations (ψ_1 and ψ_2) and fracture densities (ε_1 and ε_2) are taken to be (35^o, 108^o) and (0.03, 0.05), respectively. The objective function $J(\psi_1,\psi_2,\varepsilon_1,\varepsilon_2)$ of azimuthal fracture orientations (ψ_1,ψ_2) and fracture densities ($\varepsilon_1,\varepsilon_2$) is defined as:

$$J(\psi_1,\psi_2,\varepsilon_1,\varepsilon_2)=\frac{1}{2}\sum_{m=1}^{10}\sum_{n=1}^{12}\left[\frac{V_{mn}^{calc}(\psi_1,\psi_2,\varepsilon_1,\varepsilon_2)-V_{mn}^{obs}}{\Delta V_{mn}^{obs}}\right]^2+\frac{1}{2}\sum_{m=1}^{10}\sum_{n=1}^{12}\left[\frac{Q_{mn}^{calc}(\psi_1,\psi_2,\varepsilon_1,\varepsilon_2)-Q_{mn}^{obs}}{\Delta Q_{mn}^{obs}}\right]^2 . \quad (16)$$

The first term on the right-hand side of the objective function (equation 16) is the misfit between the observed and calculated velocity data summed over 10 different seismic frequencies and 12 azimuths, while the second term on the right-hand side is the misfit between observed and calculated attenuation data summed 10 different seismic frequencies and 12 azimuths. The velocity and attenuation data are weighted according to uncertainties in the measurements. The source of uncertainty in velocity and attenuation data is linked to measurement and processing of the seismic data.

Figure 12 shows the result of MCMc inversion for the fracture parameters using only measurements of velocity anisotropy data corresponding to different seismic frequencies and azimuths. Clearly, velocity data alone cannot recover the fracture parameters. Figure 13 shows the result of MCMc inversion for the fracture parameters, using measurements of both velocity and attenuation data corresponding to different seismic frequencies and azimuths producing the results with significantly improved certainty.

The presence of communicating aligned mesoscopic fracture sets greatly influence the anisotropic permeability on a large scale. This example shows that for the case of a fractured reservoir containing two sets of aligned mesoscopic fractures, the inverse problem does not have a unique solution if only velocity anisotropy data is used. The addition of attenuation

anisotropy data helps to resolve the non-uniqueness in the inverse problem and hence improved estimates of anisotropic permeability can be obtained.

Model 2. Aligned micro-cracks and mesoscopic fractures

The second inverse numerical example deals with the model 2 of the forward modelling section. In this case, the azimuthal variation of attenuation was only sensitive to the presence of the mesoscopic fracture set and we observed a directional variation of velocity with azimuth. In other words, the azimuthal variation of attenuation anisotropy in this case was not providing any information about the aligned micro-cracks. This suggests that the joint inversion of measurements of velocity and attenuation data corresponding to different seismic frequencies and azimuths will not be able to recover the fracture and crack density of the aligned mesoscopic fracture set and aligned set of micro-cracks, respectively.

In this example, we only demonstrate how measurements of attenuation data corresponding to different seismic frequencies and azimuths helps to resolve the non-uniqueness associated with estimation of azimuthal orientations of the mesoscopic fracture set and a set of aligned micro-cracks. The true azimuthal orientations of the mesoscopic fracture set (ψ_1) and aligned micro-cracks (ψ_c) are 35^o and 108^o, respectively. The fracture density and crack density in this example are assumed to be known and set to 0.03 and 0.05. The true values of the azimuthal orientations are estimated using the calculated velocity anisotropy data alone and also using both velocity and attenuation anisotropy data. Our objective function $J(\psi_1,\psi_c)$ of the two azimuthal orientations (ψ_1,ψ_c) is defined as:

$$J(\psi_1,\psi_c)=\frac{1}{2}\sum_{m=1}^{10}\sum_{n=1}^{12}\left[\frac{V_{mn}^{calc}(\psi_1,\psi_c)-V_{mn}^{obs}}{\Delta V_{mn}^{obs}}\right]^2+\frac{1}{2}\sum_{m=1}^{10}\sum_{n=1}^{12}\left[\frac{Q_{mn}^{calc}(\psi_1,\psi_c)-Q_{mn}^{obs}}{\Delta Q_{mn}^{obs}}\right]^2. \quad (16)$$

The first and second term on the right-hand side of the objective function (equation 16) are again the misfit between the calculated and observed seismic velocity and attenuation data

summed over 10 seismic frequencies and 12 azimuths weighted according to uncertainties in the measurements and processing of the seismic data.

Figure 14 show the MCMc inversion result in the form of posterior PDFs using either the velocity data alone or both velocity and attenuation data. The upper plots of figure 14 clearly show that the velocity anisotropy data alone cannot recover the azimuthal orientations of mesoscopic fracture set and aligned micro-cracks. The lower plots of figure 14 clearly show that using both velocity and attenuation anisotropy data resolve the non-uniqueness associated with the velocity anisotropy data alone and produces the results with considerably improved certainty.

5 Concluding Remarks

For fractured reservoir containing two sets of aligned mesoscopic fractures, one can in principle estimate the azimuthal fracture orientations and fracture densities from measurements of seismic velocity and attenuation anisotropy data corresponding to different seismic frequencies and azimuths, provided that one has priori information about the porous matrix, saturating fluid(s) and fracture geometry.

Measurements of seismic velocity anisotropy data corresponding to different seismic frequencies and azimuths may contain information about the fracture densities, but that information alone produce highly uncertain estimates and also is unable to differentiate between azimuthal fracture orientations. Joint inversion of measurements of seismic velocity and attenuation anisotropy data corresponding to different seismic frequencies and azimuths leads to improved estimates of fracture parameters and better management of fractured reservoirs.

Models consisting of aligned micro-cracks are more difficult to characterize, as azimuthal variation of attenuation is only sensitive to the presence of mesoscopic fracture sets and it can only help in resolving the non-uniqueness in azimuthal orientations of aligned

micro-cracks and mesoscopic fractures. The presence of mesoscopic fractures is more important for the reservoir scale fluid flow simulations (anisotropic permeability at large scale).

A satisfactory characterization of complex fractured reservoirs requires a model accounting for frequency-dependent anisotropy. We hope that the results obtained here should help in obtaining improved estimates of anisotropic permeability in complex fractured reservoirs systems.

Acknowledgements

PhD student Aamir Ali would like to thank Higher Education Commission (HEC), Pakistan, and Department of Earth Sciences, University of Bergen, Norway, for providing the necessary funding to complete this work. We also thank Dr. Henk Keers (Associate Professor Department of Earth Sciences, University of Bergen, Norway) for reading the manuscript.

References

Agersborg R., Jakobsen M., Ruud B.O., and Johansen T.A., 2007. Effects of pore fluid pressure on the seismic response of a fractured carbonate reservoir. Stud. Geophys. Geod. 51, 89-118.

Aster R., Borchers B., and Thurber C., 2005. Parameter estimation and Inverse Problems. Elsevier. ISBN: 0120656043.

Auld, B.A.., 1990. Acoustic Fields and Waves in Solids, Krieger Publishing, Malabar, FL.

Carcione, J.M., 1995. Constitutive model and wave equations for linear, viscoelastic, anisotropic media. Geophysics 60, 537–548.

Carcione, J.M., 2007. Wave fields in real media: Wave propagation in anisotropic, anelastic, porous and electromagnetic media: Elsevier Science Publishing Company, Inc.

Cerveny, V., and Psencik, I., 2005. Plane waves in viscoelastic anisotropic media—I. Theory. Geophys. J. Int. 161, 197–212.

Chapman, M., V. Zatsepin, S., and Crampin, S., 2002. Derivation of a microstructural poroelastic model. Geophys. J. Int. 151, 427-451.

Chapman, M., 2003. Frequency dependent anisotropy due to meso-scale fractures in the presence of equant porosity. Geophys. Prospect. 51, 369-379.

Chapman, M., 2009. Modelling the effect of multiple sets of mesoscale fractures in porous rock on frequency-dependent anisotropy. Geophysics 74, D97-D103.

Gurevich, B., Brajanovski, M., Galvin, R.J., Müller, T.M., and Toms-Stewart, J., 2009. P-wave dispersion and attenuation in fractured and porous reservoirs – poroelasticity approach. Geophys. Prospect. 57, 225-237.

Hudson, J.A., Liu, E., and Crampin, S., 1996. The mechanical properties of materials with interconnected cracks and pores. Geophys. J. Int. 124, 105-112.

Jakobsen, M., Hudson, J.A., and Johansen, T.A., 2003a. T-matrix approach to shale acoustics. Geophys. J. Int. 154, 533-558.

Jakobsen, M., Johansen, T.A., and McCann, C., 2003b. The acoustic signature of fluid flow in complex porous media. J. Appl. Geophys. 54, 219-246.

Jakobsen, M., and Chapman, M., 2009. Unified theory of global and squirt flow in cracked porous media. Geophysics 74, WA65-WA76.

Liu, E.R., Hudson, J.A., and Pointer, T., 2000. Equivalent medium representation of fractured rock. J. Geophys. Res. 105, 2981-3000.

Liu, E., Chapman, M., Zhang, Z., and Queen, J. H., 2006. Frequency-dependent anisotropy: Effects of multiple fracture sets on shear-wave polarizations. Wave Motion 44, 44-57.

Liu, E., Chapman, M., and Tod, S. R., 2007a. Analysis of travel-time and attenuation anisotropy in walkaround and walkaway VSPs from Tiguentourine field, Algeria. Extended abstract, 69th EAGE Conference and Exhibition, London UK, 11-14 June.

Liu, E., Chapman M., Varela, I., Li, X., Queen J. H., and Lynn, H., 2007b. Velocity and attenuation anisotropy: Implications of seismic fracture characterizations. The leading Edge 26**,** 1170-1174.

Maultzsch S., Chapman M., Liu E.R., and Li X.Y., 2003. Modelling frequency-dependent seismic anisotropy in fluid-saturated rock with aligned fractures: implication of fracture size estimation from anisotropic measurements. Geophys. Prospect. 51, 381-392.

Maultzsch, S., Chapman, M., Liu, E., and Li, X.Y, 2007a. Observation of anisotropic attenuation in VSP data. J. Seim. Expl. 16, 145-158.

Maultzsch, S., Chapman M., Liu E., and Li X.Y. 2007b. Modelling and analysis of attenuation anisotropy in multi-azimuth VSP data from the Clair field. Geophys. Prospect. 55, 627-642.

Müller, T.M., Gurevich, B., and Lebedev, M., 2010. Seismic wave attenuation and dispersion resulting from wave-induced flow in porous rocks - A review. Geophysics 75, 75A147-75A164.

Pointer T., Liu E.R., and Hudson J.A., 2000. Seismic wave propagation in cracked porous media. Geophys. J. Int. 142, 199-231.

Sayers, C.M., 2009. Seismic characterization of reservoirs containing multiple fracture sets. Geophys. Prospect. 48, 187-192.

Tarantola A.., 2005. Inverse Problem Theroy and Methods for Model Parameter Estimation. SIAM. ISBN 0898715725.

Tod, S., 2001. The effects on seismic waves of interconnected nearly aligned cracks. Geophys. J. Int. 146, 249-263.

Appendix-A Viscoelastic T-matrix approach to cracked porous media

The t-matrix for a cavity of type r fully saturated with a homogenous fluid is given by (Jakobsen and Chapman, 2009)

$$\mathbf{t}^{(r)} = \mathbf{t}_d^{(r)} + \mathbf{t}_d^{(r)} : \mathbf{S}^{(0)} : (\mathbf{I}_2 \otimes \boldsymbol{\psi}^{(r)}) : \mathbf{C}^{(0)}, \tag{A-1}$$

and,

$$\mathbf{t}_d^{(r)} = -\mathbf{C}^{(0)} : (\mathbf{I}_4 + \mathbf{G}^{(r)} : \mathbf{C}^{(0)})^{-1}. \tag{A-2}$$

Here, $\mathbf{S}^{(0)} = (\mathbf{C}^{(0)})^{-1}$ is the compliance tensor of the solid matrix material; $\mathbf{I}_2$ is the identity tensor for second-rank tensors; $\otimes$ is the dyadic tensor product (see Jakobsen et al., 2003), $\mathbf{G}^{(r)}$ is a fourth-rank tensor given by the strain Green's function (for a material with properties given by $\mathbf{C}^{(0)}$) integrated over a characteristic spheroid having the same shape as cavities of type r (Jakobsen and Chapman, 2009) and $\boldsymbol{\psi}^{(r)}$ is a second-rank tensor (fluid polarization tensor) that relates the fluid pressure to the applied stress. The fluid polarization tensor $\boldsymbol{\psi}^{(r)}$ is given by Jakobsen and Chapman (2009) under the assumption that the cavities are of the same scale-size and the τ-constant (squirt flow relaxation constant) is independent of shape and orientation index r. The analysis of Chapman et al., (2002) suggests that τ depends on the scale-size of the cavity, suggesting that the theory can easily be extended to model the cracked/fractured porous media under the assumption that the scale-size of fractures is much larger than that of pores and cracks. After letting the τ having an index r dependent on scale-size of the cavities the $\boldsymbol{\psi}$-tensor has the form

$$\boldsymbol{\psi}^{(r)} = \frac{-\widetilde{\boldsymbol{\Theta}} \sum_r \dfrac{\phi^{(r)} \mathbf{I}_2 : \mathbf{K}_d^{(r)}}{1 + i\omega\gamma^{(r)}\tau^{(r)}} - i\omega\tau^{(r)}\kappa_f \mathbf{I}_2 : \mathbf{K}_d^{(r)}}{1 + i\omega\gamma^{(r)}\tau^{(r)}}, \tag{A-3}$$

where,

$$\gamma^{(r)} = 1 + \kappa_f \mathbf{I}_2 : (\mathbf{K}_d^{(r)} - \mathbf{S}^{(0)}) : \mathbf{I}_2, \tag{A-4}$$

$$\mathbf{K}_d^{(r)} = (\mathbf{I}_4 + \mathbf{G}^{(r)}\mathbf{C}^{(0)})^{-1} : \mathbf{S}^{(0)}, \tag{A-5}$$

$$\widetilde{\Theta} = \kappa_f \left[\sum_r \frac{\phi^{(r)}\gamma^{(r)}}{1 + i\omega\gamma^{(r)}\tau^{(r)}} - \frac{i\Gamma_{ij}^* k_i^* k_j^* \kappa_f}{\eta_f \omega (1 - \Delta^{(r)})} \right]^{-1}, \tag{A-6}$$

and

$$\Delta^{(r)} = \frac{\Gamma_{ij}^* k_i^* k_j^* \kappa_f}{\phi \eta_f} \tau^{(r)}. \tag{A-7}$$

Here Γ_{ij}^* are the components of the effective permeability tensor of the fractured reservoir and k_i^* represents the component of the effective wave number vector, where $i, j = 1,2,3$, κ_f is the bulk modulus for the fluid, η_f is the viscosity of the fluid, ϕ is the total porosity and ω is the angular frequency of the wave, respectively. In this study we have implemented the Jakobsen and Chapman (2009) theory with a small modification in which the τ-constant is now dependent on scale-size of the inclusions and also with a modified $\widetilde{\Theta}$ term which corrects for an error related to conservation of fluid mass in Jakobsen et al., (2003b).The correction term related to global flow is given in the equation (A-7).

Appendix-B Bond transformation of the tensors

If the z-axis is parallel to the short axis of the spheroidal mesoscopic fractures or micro-cracks, then the resulting effective tensor will have the following form typical for transversely isotropic media, characterized by five independent constants:

$$\mathbf{C}^* = \begin{bmatrix} c_{11} & c_{12} & c_{13} & 0 & 0 & 0 \\ c_{12} & c_{22} & c_{13} & 0 & 0 & 0 \\ c_{13} & c_{13} & c_{33} & 0 & 0 & 0 \\ 0 & 0 & 0 & c_{44} & 0 & 0 \\ 0 & 0 & 0 & 0 & c_{44} & 0 \\ 0 & 0 & 0 & 0 & 0 & c_{66} \end{bmatrix}, \tag{B-1}$$

where

$$c_{12} = c_{11} - 2c_{66}\,. \tag{B-2}$$

If we perform a rotation of the coordinate system then the effective tensor will transform in accordance with the so-called Bond transformation law (e.g., Auld, 1990)

$$\mathbf{A}^* = \mathbf{M} : \mathbf{C}^* : \mathbf{M}^T\,, \tag{B-3}$$

where

$$\mathbf{M} = \begin{bmatrix} a_{11}a_{11} & a_{12}a_{12} & a_{13}a_{13} & 2a_{12}a_{13} & 2a_{13}a_{11} & 2a_{11}a_{12} \\ a_{21}a_{21} & a_{22}a_{22} & a_{23}a_{23} & 2a_{22}a_{23} & 2a_{23}a_{21} & 2a_{21}a_{22} \\ a_{31}a_{31} & a_{32}a_{32} & a_{33}a_{33} & 2a_{32}a_{33} & 2a_{33}a_{31} & 2a_{31}a_{32} \\ a_{21}a_{31} & a_{22}a_{32} & a_{23}a_{33} & (a_{22}a_{33}+a_{32}a_{23}) & (a_{21}a_{33}+a_{23}a_{31}) & (a_{21}a_{32}+a_{31}a_{22}) \\ a_{31}a_{11} & a_{32}a_{12} & a_{33}a_{13} & (a_{32}a_{13}+a_{12}a_{33}) & (a_{33}a_{11}+a_{13}a_{31}) & (a_{31}a_{12}+a_{11}a_{32}) \\ a_{11}a_{21} & a_{12}a_{22} & a_{13}a_{23} & (a_{12}a_{23}+a_{22}a_{13}) & (a_{13}a_{21}+a_{23}a_{11}) & (a_{11}a_{22}+a_{21}a_{12}) \end{bmatrix}, \tag{B-4}$$

and a_{ij} $(i, j = 1,2,3)$ are the elements of the rotation matrix **a**, depending the three Euler angles describing the orientation of the rotated coordinate system with respect to the original coordinate system. In a coordinate system where the fracture normal lies in the x-y plane, and the azimuthal fracture orientation (the angle between the fracture normal and the x-axis) is not identical to zero, we will need two successive rotations and two rotation matrices to obtain the corresponding effective tensor. The first one will be counterclockwise 90^o rotation around the y-axis with the following rotation matrix

$$\mathbf{a}_1 = \begin{bmatrix} 0 & 0 & -1 \\ 0 & 1 & 0 \\ 1 & 0 & 0 \end{bmatrix}. \tag{B-5}$$

The second one will be a counterclockwise arbitrary φ degree rotation around the new z-axis with the following rotation matrix

$$\mathbf{a}_2 = \begin{bmatrix} \cos\varphi & \sin\varphi & 0 \\ -\sin\varphi & \cos\varphi & 0 \\ 0 & 0 & 1 \end{bmatrix}. \tag{B-6}$$

The resulting effective tensor will have the form typical for media of monoclinic symmetry, characterized by 13 independent constants

$$\mathbf{C}^{*'} = \begin{bmatrix} c'_{11} & c'_{12} & c'_{13} & 0 & 0 & c'_{16} \\ c'_{12} & c'_{22} & c'_{23} & 0 & 0 & c'_{26} \\ c'_{13} & c'_{23} & c'_{33} & 0 & 0 & b'_{36} \\ 0 & 0 & 0 & c'_{44} & c'_{45} & 0 \\ 0 & 0 & 0 & c'_{54} & c'_{55} & 0 \\ c'_{16} & c'_{21} & c'_{36} & 0 & 0 & c'_{66} \end{bmatrix}. \tag{B-7}$$

It is important to note that the above definition of the Bond transformation is based on the Voigt representation of the fourth-rank tensors, rather than the Kelvin representation.

Appendix-C Christoffel equation for viscoelastic media

From Hooke's law the stress-strain relation can be written as using the matrix notation (Carcione, 2007)

$$\boldsymbol{\sigma} = \mathbf{C} \cdot \mathbf{e} \tag{C-1}$$

where $\boldsymbol{\sigma}$ is the stress tensor, $\mathbf{e}$ is the strain tensor and $\mathbf{C}$ is the stiffness tensor. The equation of motion in the absence of body forces can be written as (Carcione, 2007)

$$\boldsymbol{\Gamma}_{\nabla} \cdot \mathbf{u} = \rho \partial_{tt}^2 \mathbf{u}, \tag{C-2}$$

where

$$\boldsymbol{\Gamma}_{\nabla} = \nabla \cdot \mathbf{C} \cdot \nabla^T, \tag{C-3}$$

where $\mathbf{u}$ is the displacement vector and the symmetric gradient operator ∇ using the matrix representation is given by (Auld, 1990; Carcione, 2007)

$$\nabla = \begin{bmatrix} \partial_1 & 0 & 0 & 0 & \partial_3 & \partial_2 \\ 0 & \partial_2 & 0 & \partial_3 & 0 & \partial_1 \\ 0 & 0 & \partial_3 & \partial_2 & \partial_1 & 0 \end{bmatrix}. \tag{C-4}$$

The strain displacement relation is given by (Carcione, 2007)

$$\mathbf{e} = \nabla^T \cdot \mathbf{u}. \tag{C-5}$$

A general plane wave solution for the displacement vector of the body waves is given by (Carcione, 2007)

$$\mathbf{u} = \mathbf{u}_0 \exp\left[i(\omega t - \mathbf{k} \cdot \mathbf{x})\right], \tag{C-6}$$

where $\mathbf{u}_0$ represents a constant complex vector, ω is the angular frequency and $\mathbf{k}$ is the wave-number vector. The particle velocity is given by time derivative of equation (C-6) given by

$$\mathbf{v} = \partial_t \mathbf{u} = i\omega \mathbf{u}\,. \tag{C-7}$$

In the absence of body forces $(\mathbf{f} = 0)$, we consider plane waves propagating along the direction given by (Carcione, 2007)

$$\hat{\mathbf{k}} = l_1 \hat{\mathbf{e}}_1 + l_2 \hat{\mathbf{e}}_2 + l_3 \hat{\mathbf{e}}_3\,, \tag{C-8}$$

where l_1, l_1 and l_1 are the direction cosines. The wave-number vector $\mathbf{k}$ can be written as (Carcione, 2007)

$$\mathbf{k} = (k_1, k_2, k_3) = k(l_1, l_2, l_3) = k\hat{\mathbf{k}}, \tag{C-9}$$

where k is the magnitude of the wave-number vector. The spatial differential operator in equation (C-4) can be replaced by

$$\nabla \rightarrow -ik \begin{bmatrix} l_1 & 0 & 0 & 0 & l_3 & l_2 \\ 0 & l_2 & 0 & l_3 & 0 & l_1 \\ 0 & 0 & l_3 & l_2 & l_1 & 0 \end{bmatrix} \equiv -ik\mathbf{L}. \tag{C-10}$$

Now substituting the time derivative as $\partial_t \rightarrow i\omega$ and using equation (C-10) in equation (C-2), we get (Carcione, 2007)

$$k^2 \boldsymbol{\Gamma} \cdot \mathbf{u} = \rho\omega^2 \mathbf{u}, \tag{C-11}$$

where

$$\boldsymbol{\Gamma} = \mathbf{L} \cdot \mathbf{C} \cdot \mathbf{L}^T\,, \tag{C-12}$$

is the Christoffel matrix. The dispersion relation is given by (Carcione, 2007)

$$\det(\boldsymbol{\Gamma} - \rho V^2 \mathbf{I}_3) = 0. \tag{C-13}$$

where

$$V = \frac{\omega}{k}\,, \tag{C-14}$$

is the complex velocity.

The equation (C-13) is known as the Christoffel equation. Using equation (C-14), the components of the slowness and attenuation vectors can be expressed in terms of the complex velocity as (given by Carcione, 1995, 2007)

$$\mathbf{s} = \mathrm{Re}\left[\frac{1}{V}\right]\hat{\mathbf{k}}\,, \tag{C-15}$$

and

$$\alpha = -\omega\,\mathrm{Im}\left[\frac{1}{V}\right]\hat{\mathbf{k}}. \tag{C-16}$$

Table 1. Mechanical properties associated with the solid matrix and fluid (brine/water) (first and second row).

Material	Bulk Modulus (GPa)	Shear Modulus (GPa)	Density (kg/ m^3)
Solid matrix (calcite)	70	29	2710
Fluid (Water/Brine)	2.2	0.0	1000

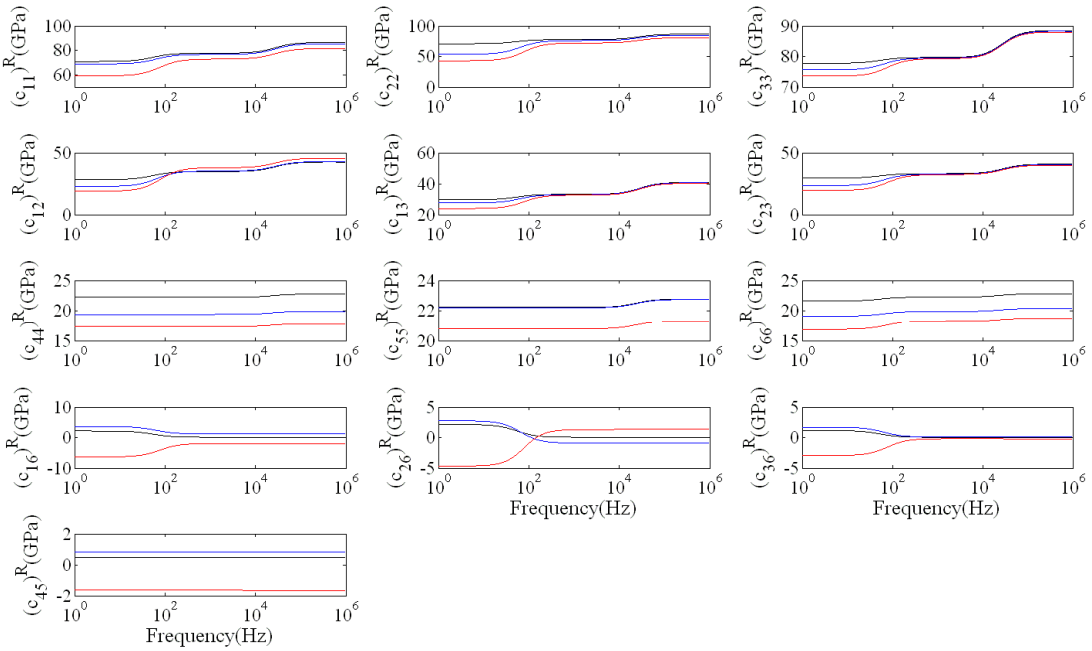

Figure 1 Real part of the independent stiffness constants as a function of frequency for different combinations of azimuthal fracture orientation and fracture densities of each individual fracture set. Black lines: (ψ_1, ψ_2, ε_1, ε_2) = (30°, 50°, 0.01, 0.03), blue lines: (ψ_1, ψ_2, ε_1, ε_2) = (50°, 75°, 0.04, 0.06) and red lines: (ψ_1, ψ_2, ε_1, ε_2) = (110°, 130°, 0.08, 0.1). The fracture radius of both the aligned mesoscopic fracture sets and matrix permeability was set to 0.1 m and 100 mD.

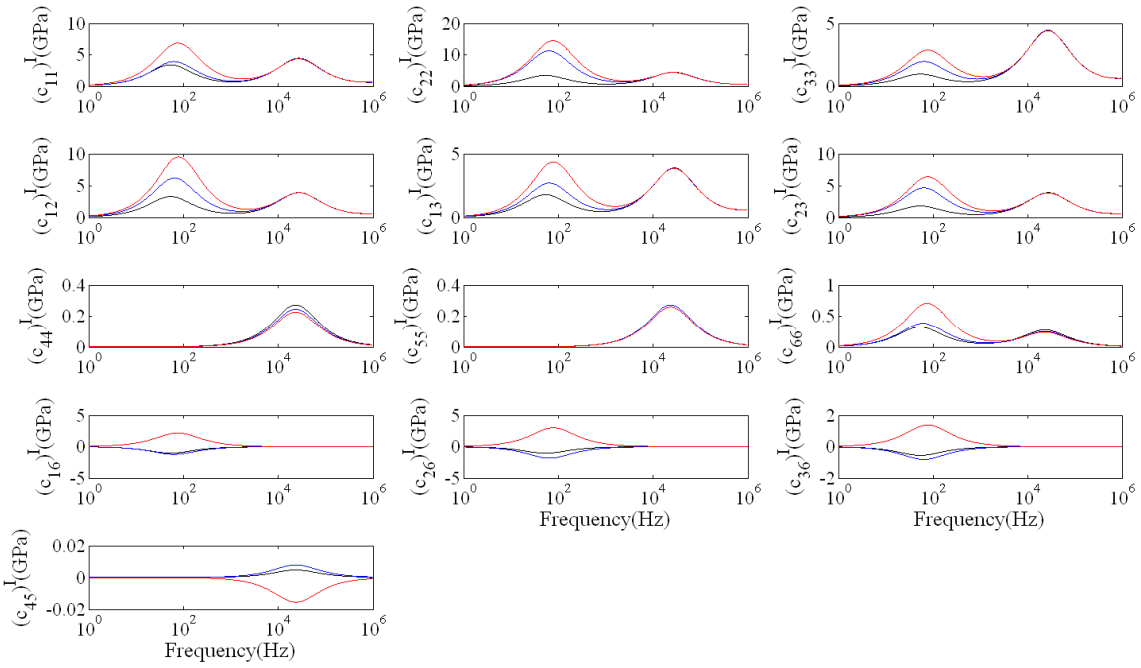

Figure 2 Same as Figure 1, but for the imaginary parts of the effective stiffness constants.

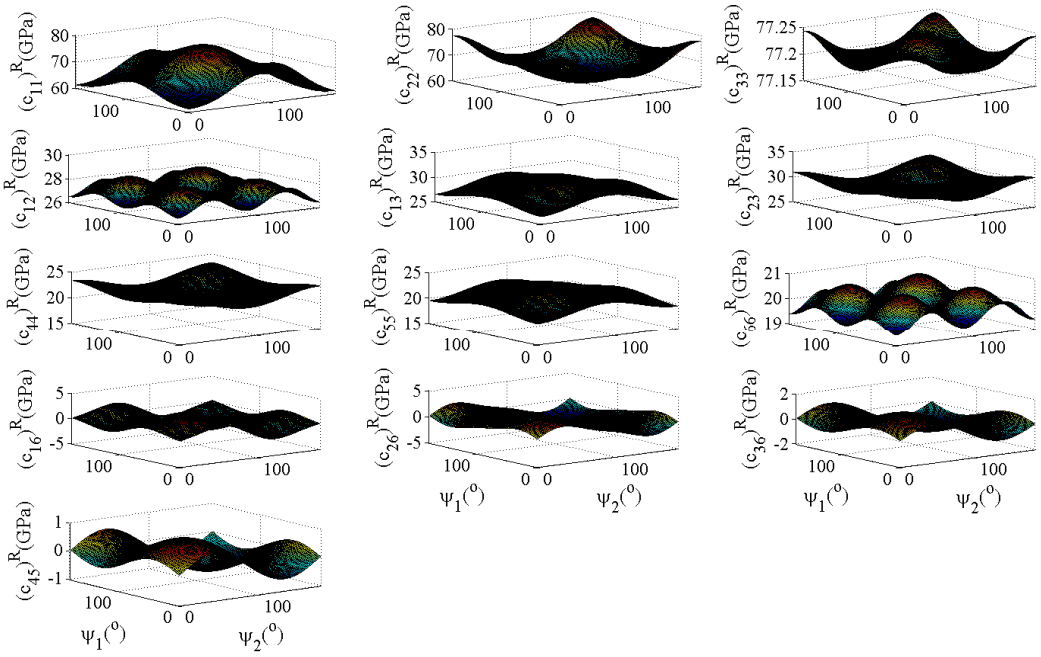

Figure 3 Real part of the independent effective stiffness constants as a function of azimuthal fracture orientations (ψ_1, ψ_2) for two fracture sets for a frequency of 40 Hz. The fracture densities for the fracture set 1 and 2 are equal to 0.03 and 0.05. The fracture radius of both the aligned mesoscopic fracture sets and matrix permeability was set to 0.1 m and 100 mD.

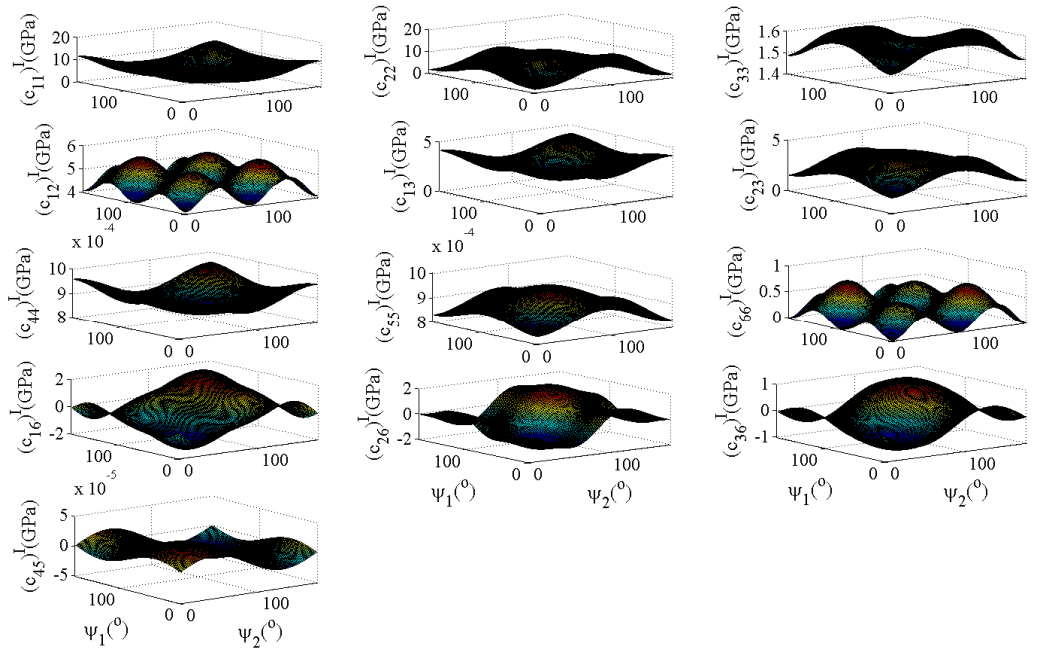

Figure 4 Same as Figure 4, but for the imaginary parts of the effective stiffness constants.

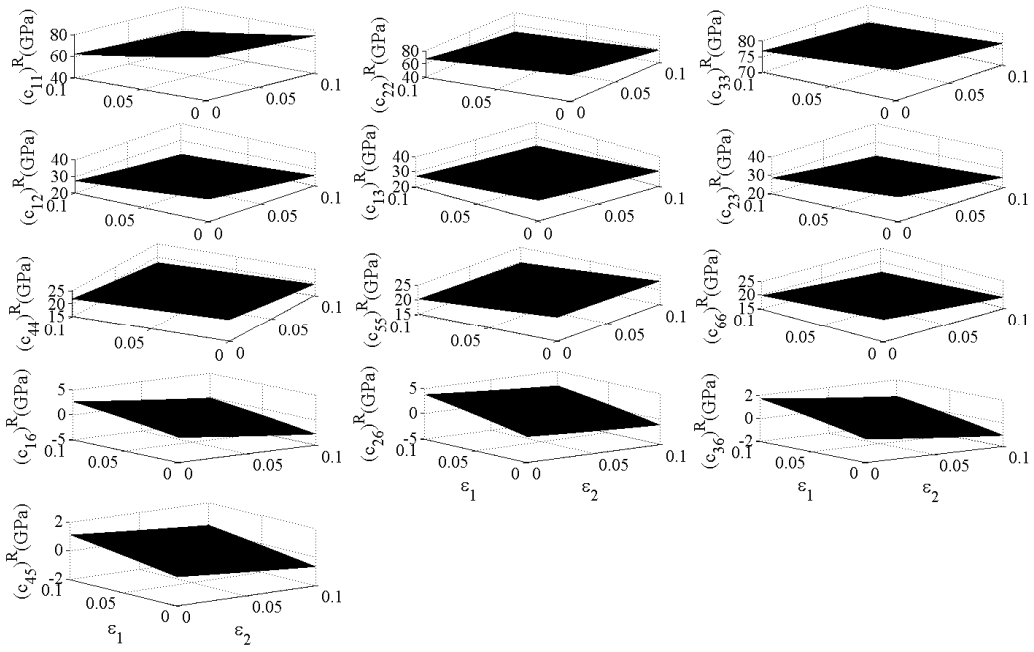

Figure 5 Real part of the independent effective stiffness constants as a function of fracture densities (ε_1, ε_2) for two fracture sets for a frequency of 40 Hz. The azimuthal orientations for fracture set 1 and 2 are equal to 35^o and 108^o. The fracture radius of both the aligned mesoscopic fracture sets and matrix permeability was set to 0.1 m and 100 mD.

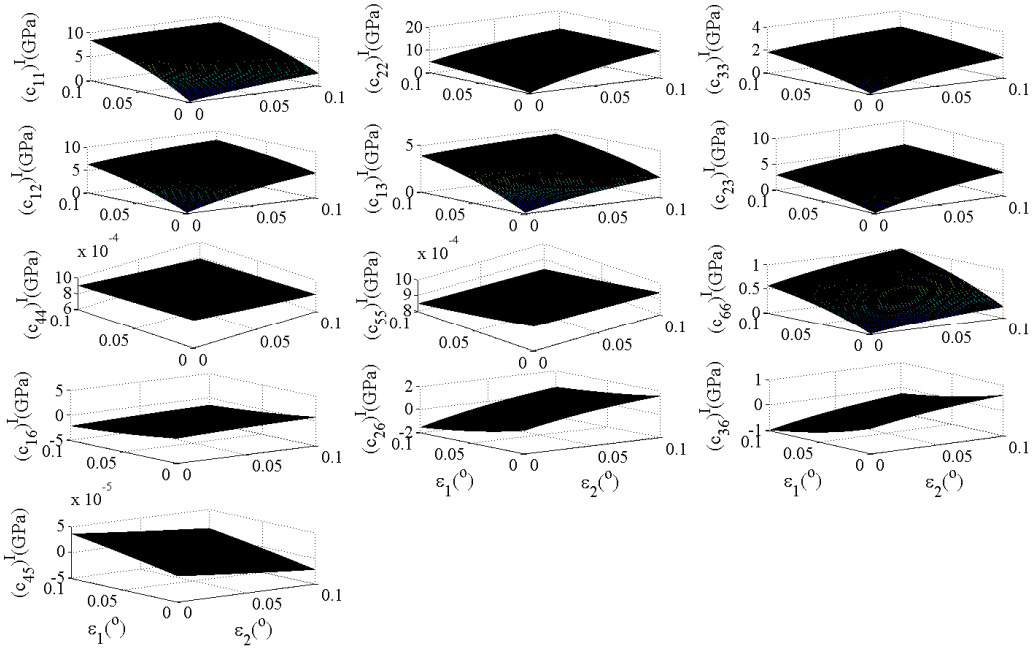

Figure 6 Same as Figure 6, but for the imaginary parts of the effective stiffness constants.

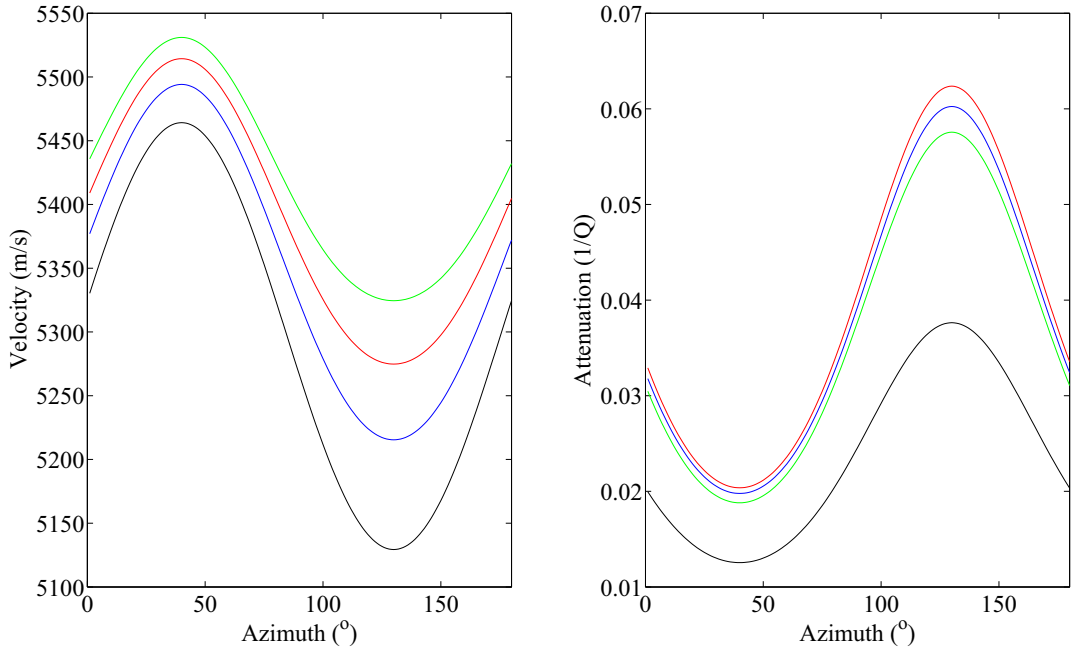

Figure 7 Azimuthal variation of P-wave velocity (left) and attenuation (right) for different seismic frequencies and a fixed polar angle of incidence (40°) in a medium with one fracture set. The azimuthal orientation of the mesoscopic fracture is 40°. Black lines: 20 Hz, blue lines: 45 Hz, red lines: 65 Hz and green lines: 90 Hz.

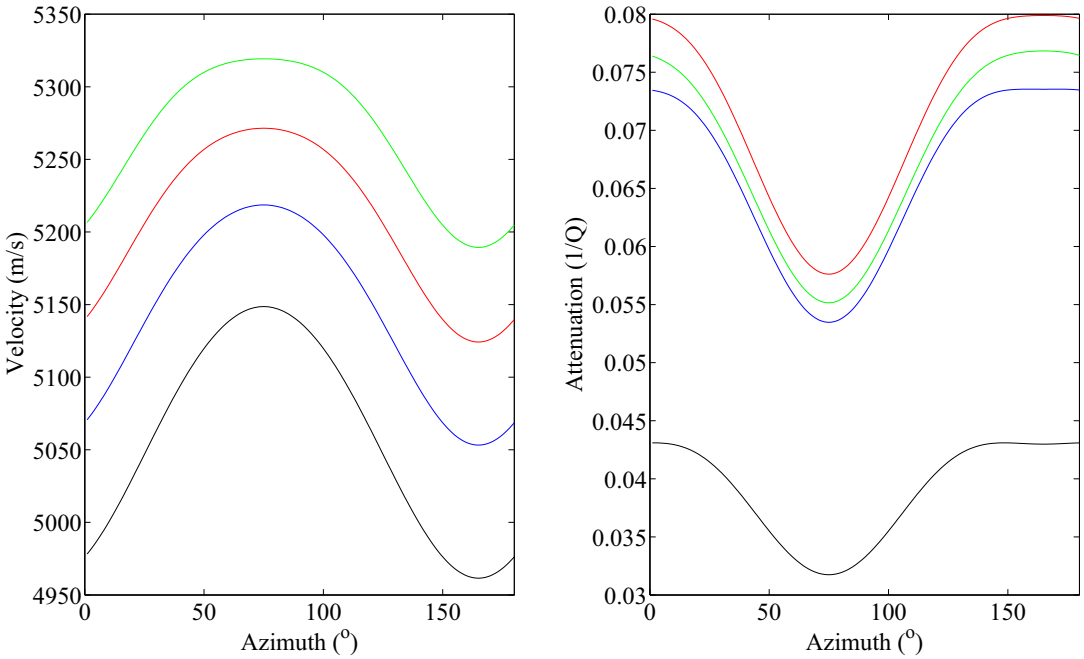

Figure 8 Azimuthal variation of P-wave velocity (left) and attenuation (right) for different seismic frequencies and a fixed polar angle of incidence (40°) in a medium with two fracture sets. The azimuthal orientations of the two mesoscopic fracture sets are 40° and 110°. Black lines: 20 Hz, blue lines: 45 Hz, red lines: 65 Hz and green lines: 90 Hz.

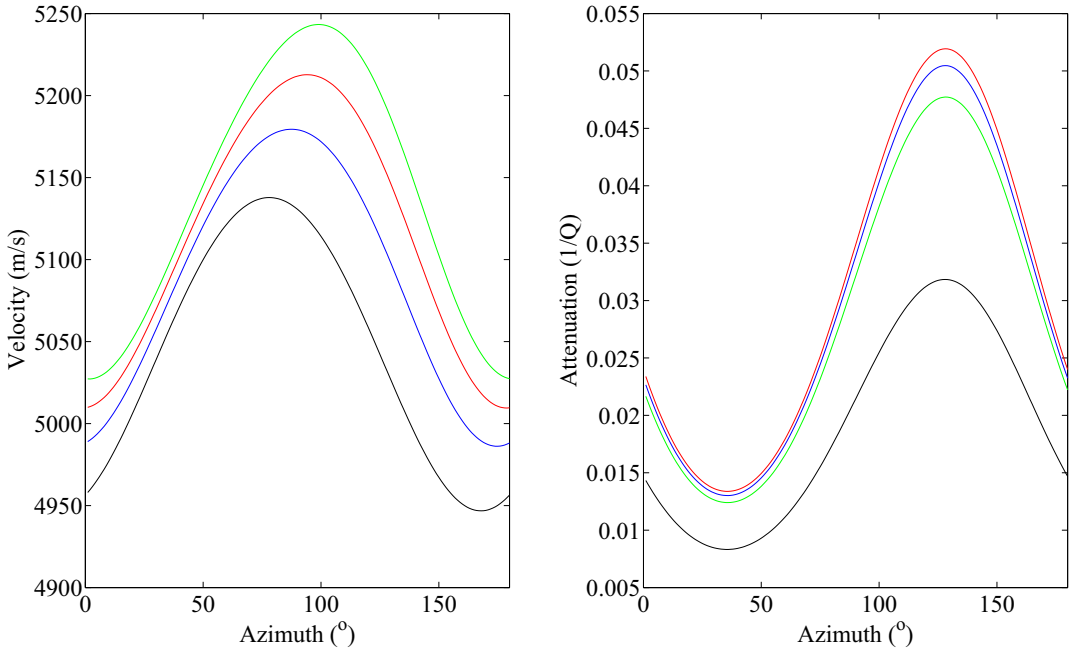

Figure 9 Same as Figure 9, but the relaxation time for one the fracture set was set equal to micro-porosity. Black lines: 20 Hz, blue lines: 45 Hz, red lines: 65 Hz and green lines: 90 Hz.

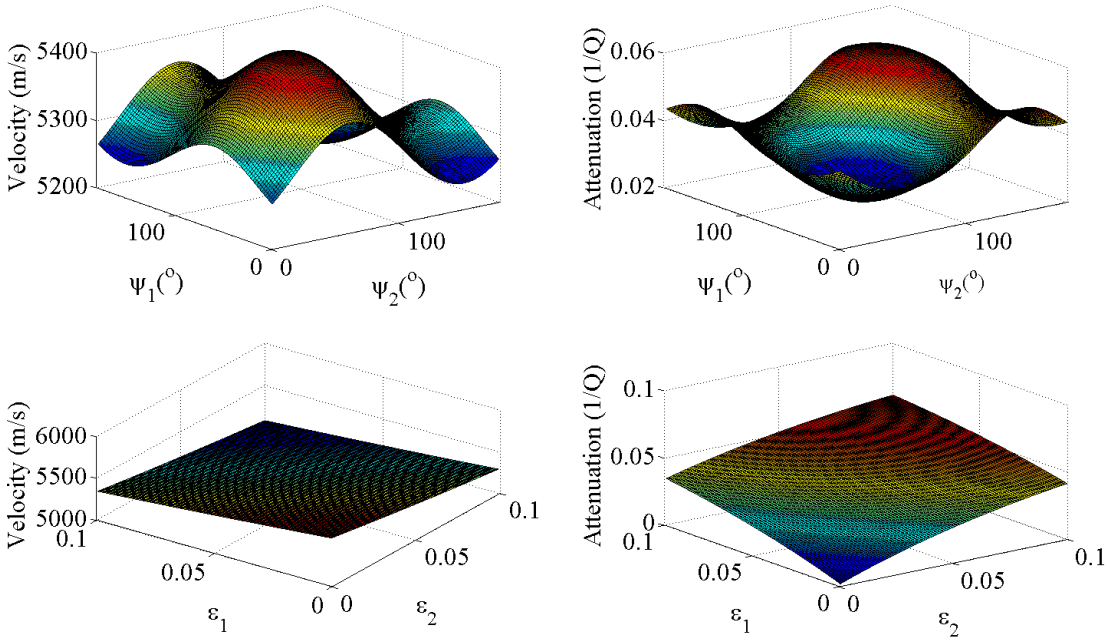

Figure 10 Predictions of velocity and attenuation as a function of fracture parameters. Upper left and right plots: predictions of velocity and attenuation as a function of two azimuthal fracture orientations (ψ_1 and ψ_2) with fracture densities of both the fracture sets equal to 0.03 and 0.05, respectively. Lower left and right plots: predictions of velocity and attenuation data as a function of two fracture densities (ε_1 and ε_2) with azimuthal fracture orientations of both the fracture sets equal to 35° and 108°, respectively.

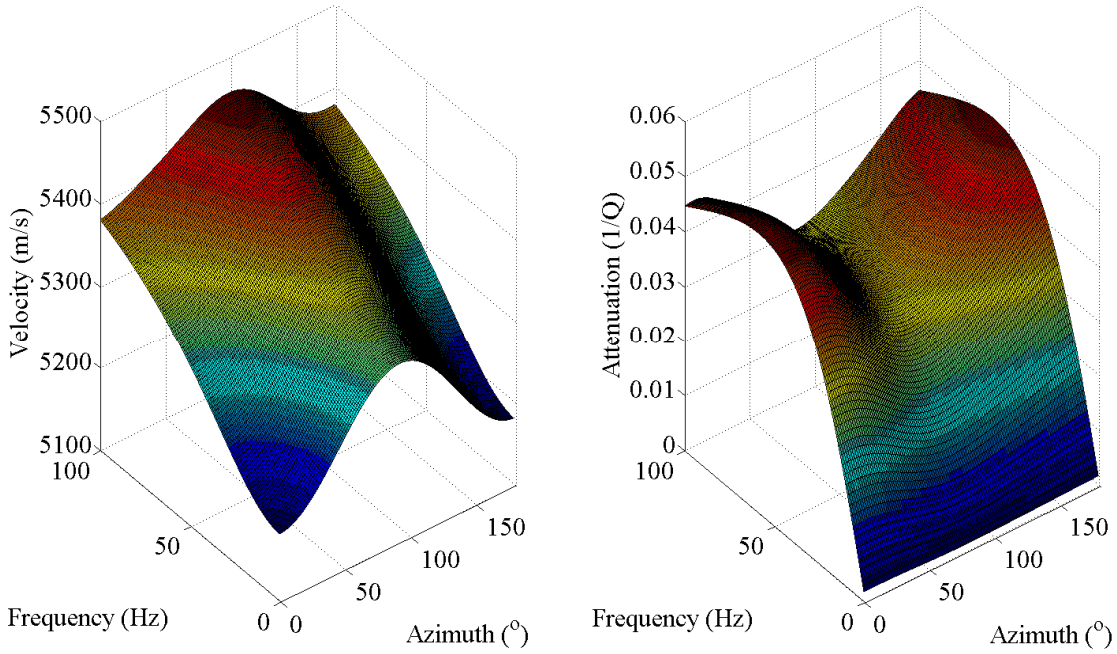

Figure 11 Seismic velocity and attenuation data as a function of seismic frequency and azimuth for a fixed polar angle of incidence (40°). The azimuthal fracture orientations (ψ_1 and ψ_2) and fracture densities (ε_1 and ε_2) of the two mesoscopic fracture sets are equal to (35°, 108°) and (0.03, 0.05) in this particular example.

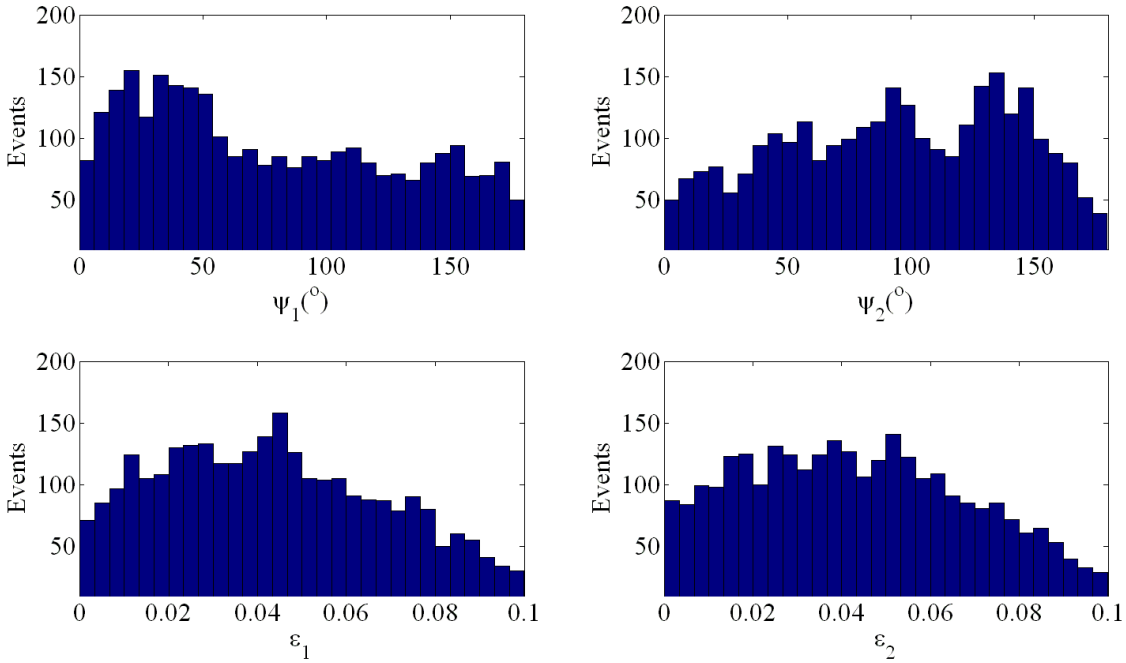

Figure 12 Samples of the marginal posterior PDF's for azimuthal fracture orientations (ψ_1 and ψ_2) and fracture densities (ε_1 and ε_2) using only measurements of seismic velocity anisotropy data corresponding to different seismic frequencies and azimuths. The standard deviation of measured seismic velocity data was set to 25%.

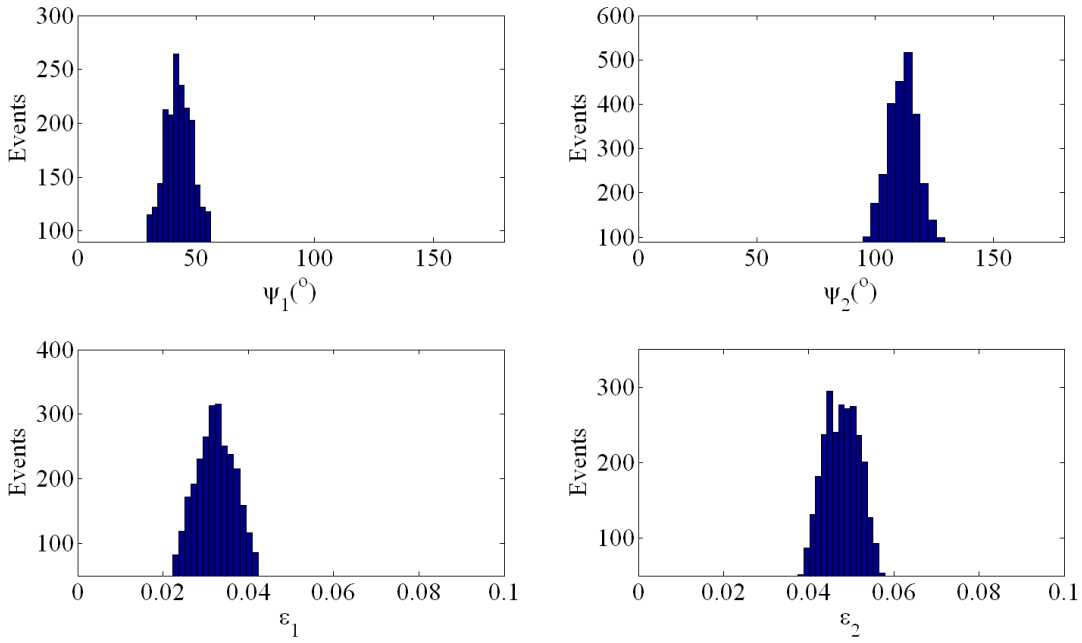

Figure 13 Samples of the marginal posterior PDF's for azimuthal fracture orientations (ψ_1 and ψ_2) and fracture densities (ε_1 and ε_2) using measurements of both seismic velocity and attenuation anisotropy data corresponding to different seismic frequencies and azimuths. The standard deviation of measured seismic velocity and attenuation data was set to 25%.

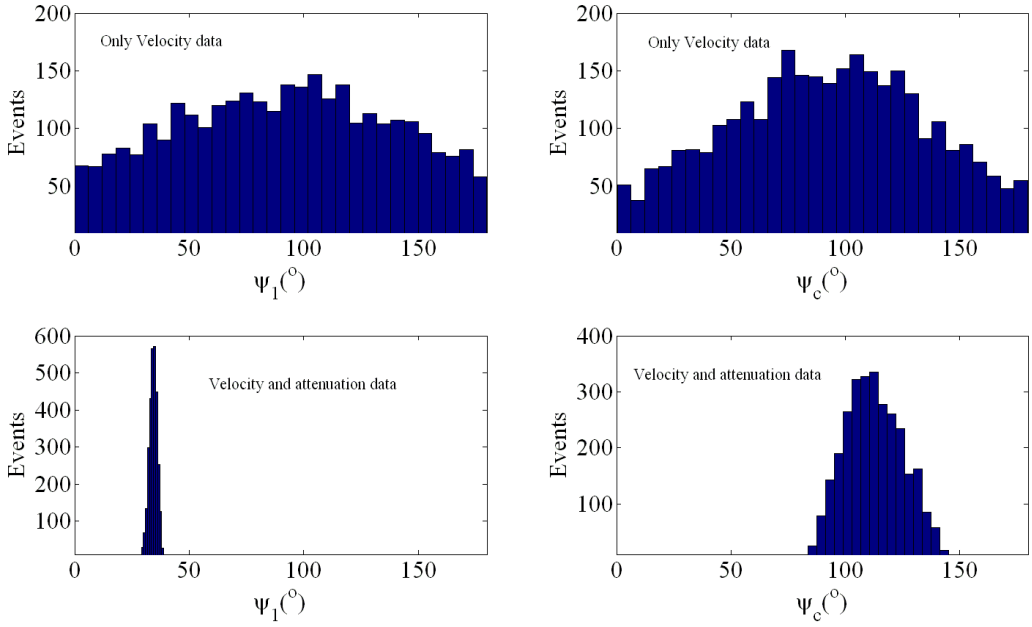

Figure 14 Samples of the marginal posterior PDF's for azimuthal orientations of mesoscopic fracture set (ψ_1) and a set of aligned cracks (ψ_c). Upper left and right plots: using only measurements of seismic velocity anisotropy data corresponding to different seismic frequencies and azimuths. Lower left and right plots: using measurements of both velocity and attenuation anisotropy data corresponding to different seismic frequencies and azimuths. The standard deviation of measured seismic velocity and attenuation data was set to 25%.